



Stabilisation of magnetic ordering in $\text{La}_3\text{Ni}_{2-x}\text{Cu}_x\text{B}'\text{O}_9$ ($\text{B}' = \text{Sb, Ta, Nb}$) by the introduction of Cu^{2+}

Chun–Mann Chin^a, Peter D. Battle^{a,*}, Emily C. Hunter^a, Maxim Avdeev^{b,c}, Mylène Hendrickx^d, Joke Hadermann^d

^a Inorganic Chemistry Laboratory, Oxford University, South Parks Road, Oxford, OX1 3QR, UK

^b Australian Nuclear Science and Technology Organisation, Lucas Heights, NSW, 2234, Australia

^c School of Chemistry, The University of Sydney, NSW, 2006, Australia

^d EMAT, University of Antwerp, Groenenborgerlaan 171, 2020, Antwerp, Belgium

ARTICLE INFO

Keywords:

Perovskite

Magnetism

Electron microscopy

ABSTRACT

$\text{La}_3\text{Ni}_{2-x}\text{Cu}_x\text{B}'\text{O}_9$ ($x = 0.25$; $\text{B}' = \text{Sb, Ta, Nb}$; $x = 0.5$; $\text{B}' = \text{Nb}$) have been synthesized and characterised by transmission electron microscopy, neutron diffraction and magnetometry. Each adopts a perovskite-like structure (space group $P2_1/n$) with two crystallographically-distinct six-coordinate sites, one occupied by a disordered arrangement of Ni^{2+} and Cu^{2+} and the other by a disordered $\sim 1:2$ distribution of Ni^{2+} and B'^{5+} , although some Cu^{2+} is found on the latter site when $x = 0.5$. Each composition undergoes a magnetic transition in the range $90 \leq T/K \leq 130$ and shows a spontaneous magnetisation at 5 K; the transition temperature always exceeds that of the $x = 0$ composition by ≥ 30 K. A long-range ordered G-type ferrimagnetic structure is present in each composition, but small relaxor domains are also present. This contrasts with the pure relaxor and spin-glass behaviour of $x = 0$, $\text{B}' = \text{Ta, Nb}$, respectively.

1. Introduction

$\text{La}_3\text{Ni}_2\text{SbO}_9$ has previously been shown [1] to adopt a monoclinic variant of the perovskite structure with two crystallographically-distinct six-coordinate sites in the unit cell. One of these is occupied exclusively by Ni^{2+} cations while the other accommodates a random 2:1 distribution of Sb^{5+} and Ni^{2+} cations, see Fig. 1. The same study revealed behaviour characteristic of a ferromagnet or ferrimagnet with a Curie temperature of 105 K. However, no evidence of long-range magnetic ordering could be detected in a neutron diffraction pattern collected at 5 K. This apparent inconsistency can be accounted for by postulating that the bulk magnetisation observed in the magnetometer arises from the presence of ferrimagnetic domains that are too small to appear ordered in a diffraction experiment conducted in zero field, but whose constituent spins are aligned by an applied magnetic field. Consistent with this explanation, a subsequent neutron diffraction study [2] showed that an increasing level of magnetic Bragg scattering is seen when the sample is subjected to an increasing applied magnetic field. That study also revealed that very weak magnetic scattering is present in the absence of a field, presumably from the largest domains in the sample. The net magnetisation within the

domains is a consequence of the unequal distribution of the magnetic Ni^{2+} cations over the two six-coordinate sites; the nearest-neighbour superexchange along a nearly-linear Ni – O – Ni pathway will always be antiferromagnetic, but the spin-up cations outnumber those with spin-down by a factor of two. By analogy with the relaxor ferroelectric $\text{Pb}_3\text{MgNb}_2\text{O}_9$ [3], $\text{La}_3\text{Ni}_2\text{SbO}_9$ was classified as a relaxor ferromagnet.

In an attempt to increase the temperature of the relaxor transition we have previously investigated the consequences of replacing Sb^{5+} by Ta^{5+} , Nb^{5+} , W^{6+} and Te^{6+} . Neither $\text{SrLa}_2\text{Ni}_2\text{TeO}_9$ [4] nor $\text{CaLa}_2\text{Ni}_2\text{WO}_9$ [5] show behaviour similar to that of $\text{La}_3\text{Ni}_2\text{SbO}_9$; in each case $\chi(T)$ suggests that a spin glass forms below ~ 30 K, although this is an oversimplified description of the tellurium-containing composition. $\text{La}_3\text{Ni}_2\text{NbO}_9$ also forms a spin-glass phase below 29 K [6,7] but $\text{La}_3\text{Ni}_2\text{TaO}_9$ shows [6] the same type of behaviour as $\text{La}_3\text{Ni}_2\text{SbO}_9$, albeit with a lower transition temperature of ~ 85 K. In this case no magnetic Bragg scattering could be detected in a neutron diffraction pattern collected at 5 K in the absence of an applied field, making $\text{La}_3\text{Ni}_2\text{TaO}_9$ perhaps the best example of a relaxor ferromagnet identified to date. Other studies, conducted by ourselves and others, have investigated the consequences of replacing Ni^{2+} by other magnetic cations. $\text{LaSr}_2\text{Cr}_2\text{SbO}_9$ [8] and $\text{SrLa}_2\text{FeCoSbO}_9$

* Corresponding author.

E-mail address: peter.battle@chem.ox.ac.uk (P.D. Battle).

<https://doi.org/10.1016/j.jssc.2019.05.006>

Received 3 April 2019; Received in revised form 6 May 2019; Accepted 6 May 2019

Available online 9 May 2019

0022-4596/© 2019 The Authors. Published by Elsevier Inc. This is an open access article under the CC BY license (<http://creativecommons.org/licenses/by/4.0/>).

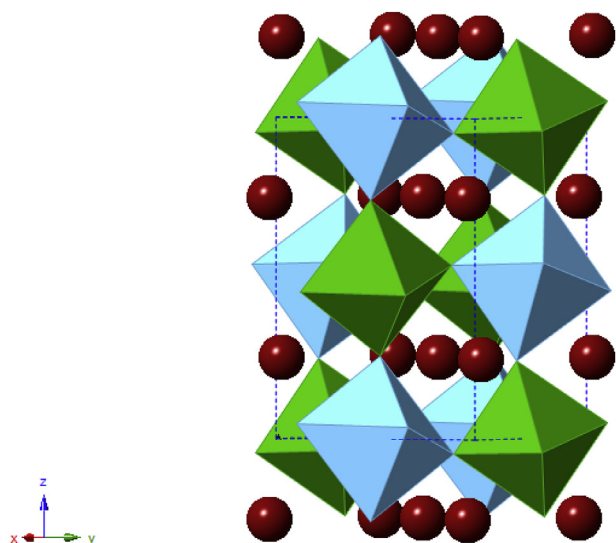


Fig. 1. Crystal structure of $\text{La}_3\text{Ni}_2\text{SbO}_9$. Green octahedra are occupied Ni^{2+} ; blue octahedra by Ni^{2+} and Sb^{5+} . Red circles represent La^{3+} cations at the A site. (For interpretation of the references to colour in this figure legend, the reader is referred to the Web version of this article.)

[9] both show long-range ferrimagnetism, with transition temperatures of 190 and 240 K, respectively, whereas Franco et al. have reported [10] significant magnetic frustration and an absence of long-range magnetic order in $\text{La}_3\text{Co}_2\text{SbO}_9$.

It is thus clear that the magnetic properties of these triple perovskites are very sensitive to chemical composition. In our opinion the contrast between the spin-glass behaviour of $\text{La}_3\text{Ni}_2\text{NbO}_9$ and the relaxor behaviour of $\text{La}_3\text{Ni}_2\text{TaO}_9$ is particularly striking. A study of solid solutions in the system $\text{La}_3\text{Ni}_2\text{Sb}_x\text{Ta}_y\text{Nb}_{1-x-y}\text{O}_9$ showed [11] that the introduction of niobium destroys the magnetisation observed in the compositions $x = 1, y = 0$ and $x = 0, y = 1$ and leads to the formation of a spin glass in each case. In this paper we report the surprising consequences of partially replacing the Ni^{2+} cations in $\text{La}_3\text{Ni}_2\text{B}'\text{O}_9$ ($\text{B}' = \text{Sb}, \text{Nb}, \text{Ta}$) by Cu^{2+} cations.

2. Experimental

The traditional ceramic method was used to synthesise polycrystalline samples of $\text{La}_3\text{Ni}_{2-x}\text{Cu}_x\text{B}'\text{O}_9$ for $x = 0.25$; $\text{B}' = \text{Sb}, \text{Ta}$ or Nb and $x = 0.5$; $\text{B}' = \text{Nb}$. Mixtures containing analytical-grade NiO , CuO , $\text{B}'_2\text{O}_5$ ($\text{B}' = \text{Sb}, \text{Ta}$ or Nb) and pre-dried La_2O_3 in a stoichiometric ratio were thoroughly ground in an agate mortar and pestle, and then pelletised before being heated at 1100 or 1200 °C for several periods of two or three days. After each heating the pellets were ground up and then reformed. Different compositions needed a different number of heating cycles to optimise the purity of the perovskite but a typical synthesis took 5–6 cycles.

A PANalytical Empyrean diffractometer was used to record the X-ray powder diffraction (XRPD) patterns of the reaction products at room temperature. Data were collected, using $\text{Cu } K_{\alpha 1}$ radiation ($\lambda = 1.54051 \text{ \AA}$), over the angular range $15 \leq 2\theta/^\circ \leq 125$ with a step-size, $\Delta 2\theta$, of 0.0066° . Ni^{2+} and Cu^{2+} possess a similar number of electrons and, consequently, XRPD cannot distinguish between these cations. Conversely, the neutron scattering lengths of Ni and Cu, 10.3 and 7.72 fm, respectively, provide substantial contrast. Neutron powder diffraction (NPD) patterns were therefore collected at various temperatures using the diffractometer ECHIDNA [12] at ANSTO, Australia. Data were collected over the angular range $10 \leq 2\theta/^\circ \leq 158$ with $\Delta 2\theta = 0.05^\circ$. Wavelengths of 1.622 and 2.4395 Å were used, the latter in order to ensure that weak magnetic scattering at relatively long d -spacings was not overlooked. All diffraction patterns were analysed using the Rietveld

method [13], as implemented in the GSAS program suite [14]. A 15-term shifted Chebyshev function and a pseudo-Voigt function were employed to model the background level and peak shapes respectively.

The composition and homogeneity of each sample was studied by means of analytical transmission electron microscopy (TEM). The specimen was prepared by dispersing a crushed powder sample in ethanol and depositing a few drops of this suspension on a holey carbon film covering a molybdenum grid. Energy-dispersive X-ray (EDX) elemental maps were acquired using an FEI Osiris microscope equipped with a Super-X detector and operated at 200 kV. The intensities of the K lines were used to quantify the Cu and Ni content of each sample whereas the L lines were used to quantify La, Nb, Sb and Ta. In order to assess the homogeneity both from particle to particle and within an individual particle, different regions of a number of different particles were analysed. For each sample, a total of at least thirty regions were assessed. A more detailed electron-microscopy study was carried out on $\text{La}_3\text{Ni}_{1.75}\text{Cu}_{0.25}\text{NbO}_9$. Selected-area electron diffraction (SAED) and convergent-beam electron diffraction (CBED) patterns were collected using a CM20 microscope. High-angle, annular dark field scanning TEM (HAADF-STEM) images and high-resolution EDX (HR-EDX) analyses were acquired using an FEI Titan 80–300 “cubed” microscope equipped with a Super-X detector and operated at 300 kV and 200 kV for HAADF-STEM and HR-EDX, respectively.

The magnetic properties of these copper-doped perovskites were characterised using a SQUID magnetometer. The temperature dependence of the dc molar magnetic susceptibility, $\chi(T)$, was measured in a magnetic field of 100 Oe over a temperature range of $2 \leq T/\text{K} \leq 300$ under both zero-field-cooled (ZFC) and field-cooled (FC) conditions. The ac susceptibility was measured in an oscillating field of amplitude 3.5 Oe over the temperature range $2 \leq T/\text{K} \leq 150$ at frequencies, ω , of 1, 10, 100 and 1000 Hz. The magnetisation per formula unit (f.u.) was measured as a function of applied field and temperature. The field was cycled through the range $-50 \leq H/\text{kOe} \leq 50$ at temperatures selected after consideration of the results of the dc and ac susceptibility measurements.

3. Results

The XRPD data showed that the principal component of each reaction product was a perovskite-like phase, see Fig. S1. Weak, additional reflections revealed the presence of minor impurity phases which were identified as diamagnetic $\text{La}_3\text{B}'\text{O}_7$ ($\text{B}' = \text{Sb}, \text{Ta}$ or Nb) [15–18] and $\text{LaNb}_{1-y}\text{Ta}_y\text{O}_4$. The concentration of the impurity phases increased when we attempted to prepare compositions containing a higher concentration of copper. Preliminary analysis of the patterns suggested that, in common with many related compounds studied previously [19,20], all the perovskite phases crystallise in the monoclinic space group $P2_1/n$ with $a \sim b \sim \sqrt{2}a_p$, $c \sim 2a_p$ and $\beta \sim 90^\circ$ where a_p is the cell parameter of a primitive cubic perovskite. Comparison with the results of our earlier work [6] showed that several of the relatively-broad maxima seen in the diffraction patterns of the Cu-free compositions, for example $\text{La}_3\text{Ni}_2\text{TaO}_9$, are split in the patterns collected from the Cu-doped compounds, showing that the non-cubic strain is greater in the latter. The fits to our XRPD data shown in Fig. S1 are based on a model in which the $2c$ sites are predominantly ($\sim 98\%$) occupied by divalent d -block cations and the $2d$

Table 1

Metal content (atomic %) of $\text{La}_3\text{Ni}_{2-x}\text{Cu}_x\text{B}'\text{O}_9$ ($x = 0.25$ or 0.5 ; $\text{B}' = \text{Sb}, \text{Ta}$ or Nb) determined by STEM-EDX.

Sample	% La	% Ni	% Cu	% B'
$\text{La}_3\text{Ni}_{1.75}\text{Cu}_{0.25}\text{SbO}_9^a$	50.5 ± 2.1	28.3 ± 1.7	5.0 ± 0.6	16.3 ± 1.0
$\text{La}_3\text{Ni}_{1.75}\text{Cu}_{0.25}\text{TaO}_9^a$	51.0 ± 1.4	27.3 ± 1.4	4.3 ± 1.0	17.5 ± 1.5
$\text{La}_3\text{Ni}_{1.75}\text{Cu}_{0.25}\text{NbO}_9^a$	51.9 ± 1.2	29.4 ± 1.0	4.7 ± 0.5	14.1 ± 1.3
$\text{La}_3\text{Ni}_{1.5}\text{Cu}_{0.5}\text{NbO}_9^b$	52.8 ± 0.6	24.1 ± 0.6	8.3 ± 0.3	14.7 ± 0.7

^a Expected; La 50, Ni 29.17, Cu 4.17, B' 16.66.

^b Expected; La 50, Ni 25, Cu 8.33, Nb 16.67.

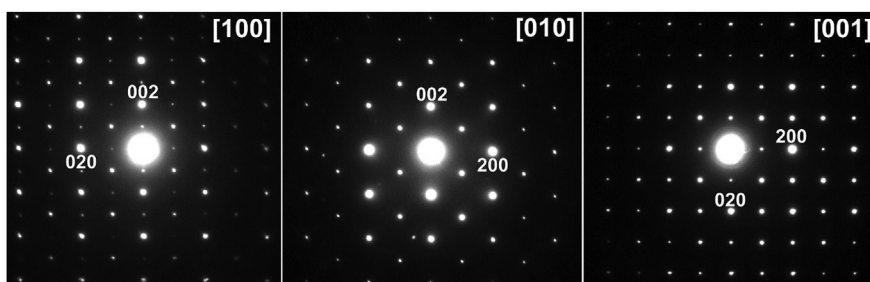


Fig. 2. SAED patterns of $\text{La}_3\text{Ni}_{1.75}\text{Cu}_{0.25}\text{NbO}_9$ taken along the zone axes [100], [010] and [001].

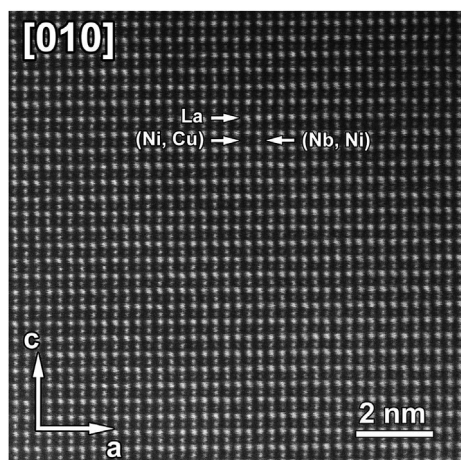


Fig. 3. High resolution HAADF-STEM image of $\text{La}_3\text{Ni}_{1.75}\text{Cu}_{0.25}\text{NbO}_9$ along the [010] zone axis, where the continuous rows of bright dots along the a -axis are occupied by La. The rows with alternation of darker and brighter dots along the a -axis correspond to (Ni, Cu) and (Nb, Ni) atom columns, respectively.

sites by a random distribution of divalent and pentavalent cations. The La^{3+} cations occupy a $4e$ site and the oxide anions are distributed over three such sites.

The results of our STEM-EDX analyses are summarized in Table 1. Some particles with a La:Nb ratio of 3:1 or 1:1 were identified, which is consistent with the results of our X-ray diffraction experiments. However, significant deviations from the ideal composition were found in only a negligible number of particles and the samples can be considered to be homogeneous. The SAED patterns of $\text{La}_3\text{Ni}_{1.75}\text{Cu}_{0.25}\text{NbO}_9$ taken along the main zone axes [100], [010] and [001] can be indexed, see Fig. 2, using the cell parameters $a \approx b \approx \sqrt{2}a_p$, $c \approx 2a_p$, where a_p is

the unit cell parameter of a primitive cubic perovskite, and $\alpha, \beta, \gamma \approx 90^\circ$. Using a combination of SAED, CBED and HAADF-STEM, the space group $P2_1/n$ was conclusively derived from the TEM data, details can be found in the Supporting Information. The [010] HAADF-STEM image shown in Fig. 3 shows that a high degree of cation ordering is present in this sample. The continuous rows of bright dots along the a -axis corresponds to columns of La^{3+} cations. The rows showing an alternation of brighter and darker dots along the a -axis correspond to alternating (Nb, Ni) and (Ni, Cu) columns respectively. (The intensity of the atom columns is proportional to the atomic number of the elements: $I \sim Z^2$.) The preference of the Cu^{2+} cations for the Ni^{2+} -rich $2c$ sites is shown by the atomic-resolution EDX maps in Fig. 4. The A-site La^{3+} cations are indicated in red and the Ni^{2+} , Cu^{2+} and Nb^{5+} cations on the B sites are mapped in green, yellow and blue, respectively. $\text{La}_3\text{Ni}_{1.75}\text{Cu}_{0.25}\text{NbO}_9$ is seen to have Nb^{5+} cations on alternate sites along [100] rows, whereas Ni^{2+} is present on all B sites, but with a greater abundance on the sites not occupied by Nb^{5+} . The Cu^{2+} cations are less clearly mapped because of their low concentration in the compound, but it can be seen that they are predominantly found on the Ni-rich sites. This is best seen by comparing the overlapped Ni-Cu and Nb-Cu maps shown in Fig. 4.

The NPD patterns collected at room temperature (RT) using $\lambda = 1.622 \text{ \AA}$ were analysed in order to determine if there was any Ni/Cu ordering over the B-site. The resulting fits are shown in Figs. 5 and S4. Consistent with the analysis of the XRPD and TEM data reported above, it was found that the dominant perovskite phase in each compound adopts the space group $P2_1/n$ and that these compositions were contaminated with minimal (less than 1 wt %) diamagnetic impurities, namely $\text{La}_3\text{B}'\text{O}_7$ ($\text{B}' = \text{Sb, Ta or Nb}$) and $\text{LaNb}_{1-y}\text{Ta}_y\text{O}_4$. On the basis of the model derived from the XRPD data, the pentavalent cations were assigned to the $2d$ site only, whereas the distribution of Ni^{2+} and Cu^{2+} over the $2c$ and $2d$ sites was allowed to vary so as to determine any site preference between these two cations. Our preliminary refinements showed that, except in the case of $\text{La}_3\text{Ni}_{1.5}\text{Cu}_{0.5}\text{NbO}_9$, the Cu^{2+} cations only occupy the $2c$ site and they were excluded from the $2d$ site in our final refinements. The structural

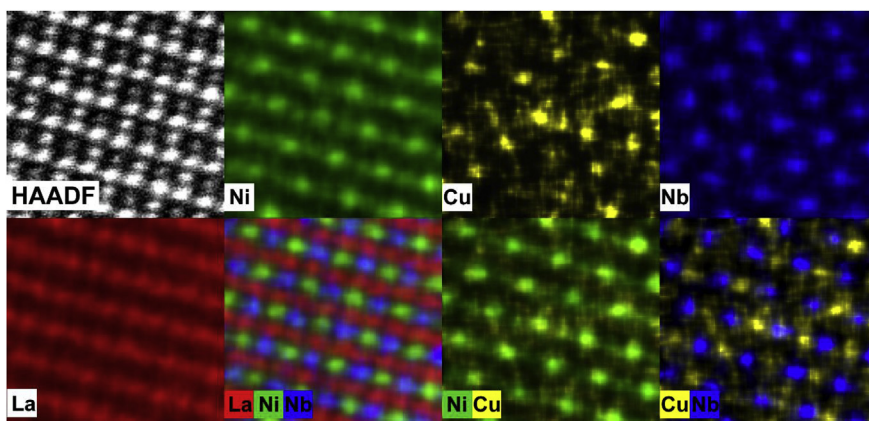


Fig. 4. High-resolution HAADF-STEM image of $\text{La}_3\text{Ni}_{1.75}\text{Cu}_{0.25}\text{NbO}_9$ along [010] (top left) and atomic-resolution EDX maps, acquired for 17 min. Partial ordering is present between Ni and Nb, and Cu is located at the six-coordinate sites containing most Ni.

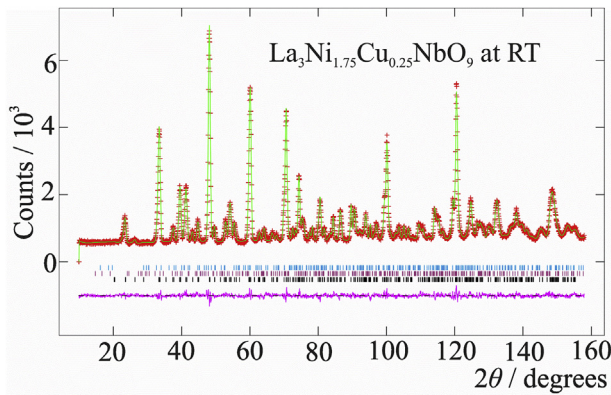


Fig. 5. Observed (red crosses) and calculated (green line) NPD profiles of $\text{La}_3\text{Ni}_{1.75}\text{Cu}_{0.25}\text{NbO}_9$ at room temperature. A difference curve (purple) is shown below. Reflection positions are marked for LaNbO_4 (top, cyan), La_3NbO_7 (middle, purple) and the principal perovskite phase (bottom, black). (For interpretation of the references to colour in this figure legend, the reader is referred to the Web version of this article.)

model, see Tables 2, S1 and S2, that has been derived from the NPD data collected at room temperature for the 12.5% Cu-substituted compositions thus has Ni^{2+} and Cu^{2+} occupying the 2c sites and the remaining Ni^{2+} cations and the pentavalent B^{5+} cations occupying the 2d sites. This is consistent with the high-resolution EDX map of $\text{La}_3\text{Ni}_{1.75}\text{Cu}_{0.25}\text{NbO}_9$ described above and shown in Fig. 4. In the case of $\text{La}_3\text{Ni}_{1.5}\text{Cu}_{0.5}\text{NbO}_9$, the 2c site was found to contain Ni^{2+} and Cu^{2+} and 2d sites Ni^{2+} , Cu^{2+} and Nb^{5+} , see Table 3. The bond lengths and bond angles derived from our analyses of the neutron diffraction data are listed in Tables 4 and 5.

The temperature dependence of the ZFC and FC molar magnetic susceptibility of $\text{La}_3\text{Ni}_{1.75}\text{Cu}_{0.25}\text{B}'\text{O}_9$ ($\text{B}' = \text{Sb}, \text{Nb}$ or Ta) and $\text{La}_3\text{Ni}_{1.5}\text{Cu}_{0.5}\text{NbO}_9$ in an applied field of 100 Oe is shown in Fig. 6. The data from all four compounds show the same general trends; the ZFC and FC curves

Table 2
Structural parameters of $\text{La}_3\text{Ni}_{1.75}\text{Cu}_{0.25}\text{NbO}_9$ at RT and 3 K (Space group $P2_1/n$).

		RT	3 K
$a/\text{\AA}$		5.5890(1)	5.5769(1)
$b/\text{\AA}$		5.6516(1)	5.6503(1)
$c/\text{\AA}$		7.9194(2)	7.9049(2)
$\beta/^\circ$		90.04(1)	90.04(1)
$V/\text{\AA}^3$		250.15(1)	249.09(1)
$R_{\text{wp}} \text{NPD}/\%$		4.10	3.84
χ^2		1.565	1.985
La	x	0.4915(6)	0.4910(4)
4e (x y z)	y	0.4593(2)	0.4571(2)
	z	0.246(1)	0.253(1)
	$U_{\text{iso}}/\text{\AA}^2$	0.0185(4)	0.0149(3)
Ni/Cu/Nb1	$U_{\text{iso}}/\text{\AA}^2$	0.0036(2)	0.0011(2)
2c (0 1/2 0)	Ni occupancy	0.833	0.833
	Cu occupancy	0.167	0.167
	Nb occupancy	0	0
Ni/Cu/Nb2	$U_{\text{iso}}/\text{\AA}^2$	0.0036(2)	0.0011(2)
2d (1/2 0 0)	Ni occupancy	0.333	0.333
	Cu occupancy	0	0
	Nb occupancy	0.667	0.667
O1	x	0.793(1)	0.796(1)
4e (x y z)	y	0.797(1)	0.798(1)
	z	−0.0365(7)	−0.0378(6)
	$U_{\text{iso}}/\text{\AA}^2$	0.003(1)	0
O2	x	0.711(1)	0.712(1)
4e (x y z)	y	0.282(1)	0.283(1)
	z	−0.0465(8)	−0.0453(7)
	$U_{\text{iso}}/\text{\AA}^2$	0.015(1)	0.011(1)
O3	x	0.5786(5)	0.5801(4)
4e (x y z)	y	0.0185(4)	0.0179(3)
	z	0.244(1)	0.247(1)
	$U_{\text{iso}}/\text{\AA}^2$	0.0153(6)	0.0111(5)

Table 3

Structural parameters of $\text{La}_3\text{Ni}_{1.5}\text{Cu}_{0.5}\text{NbO}_9$ at RT and 3 K (Space group $P2_1/n$).

		RT	3 K
$a/\text{\AA}$		5.5915(1)	5.5793(1)
$b/\text{\AA}$		5.6617(1)	5.6617(1)
$c/\text{\AA}$		7.9203(2)	7.9055(2)
$\beta/^\circ$		90.06(1)	90.05(1)
$V/\text{\AA}^3$		250.74(1)	249.72(1)
$R_{\text{wp}} \text{NPD}/\%$		4.18	3.90
χ^2		2.140	2.651
La	x	0.4906(5)	0.4906(4)
4e (x y z)	y	0.4586(2)	0.4566(2)
	z	0.252(1)	0.253(1)
	$U_{\text{iso}}/\text{\AA}^2$	0.0177(3)	0.0140(3)
Ni/Cu/Nb1	$U_{\text{iso}}/\text{\AA}^2$	0.0037(2)	0.0013(2)
2c (0 1/2 0)	Ni occupancy	0.80(5)	0.80
	Cu occupancy	0.20(5)	0.20
	Nb occupancy	0	0
Ni/Cu/Nb2	$U_{\text{iso}}/\text{\AA}^2$	0.0037(2)	0.0013(2)
2d (1/2 0 0)	Ni occupancy	0.20(5)	0.20
	Cu occupancy	0.13(5)	0.13
	Nb occupancy	0.667	0.667
O1	x	0.791(1)	0.792(1)
4e (x y z)	y	0.799(1)	0.800(1)
	z	−0.0356(6)	−0.0377(5)
	$U_{\text{iso}}/\text{\AA}^2$	0.006(1)	0
O2	x	0.707(1)	0.707(1)
4e (x y z)	y	0.284(1)	0.285(1)
	z	−0.0462(6)	−0.0459(6)
	$U_{\text{iso}}/\text{\AA}^2$	0.011(1)	0.012(1)
O3	x	0.5806(4)	0.5819(3)
4e (x y z)	y	0.0187(4)	0.0202(3)
	z	0.252(1)	0.252(1)
	$U_{\text{iso}}/\text{\AA}^2$	0.0152(5)	0.0103(4)

do not overlie below 100 K and both the ZFC and FC molar susceptibilities decrease sharply on heating through the temperature range $75 \leq T/\text{K} \leq 150$. Note that under FC conditions $\chi_{\text{MAX}} > 15 \text{ cm}^3 \text{ mol}^{-1}$ for all compositions. These compounds appear to be paramagnetic above 200 K, where $\chi^{-1}(T)$ is linear. The data collected in the range $200 \leq T/\text{K} \leq 300$ were fitted to the Curie–Weiss law to yield the molar Curie constant, C_m , and the Weiss temperature θ_W . These parameters are listed in Table 6. The former has contributions from both the Ni^{2+} and Cu^{2+} cations and the observed values, C_m , are therefore compared to the calculated value, C_m^{calc} , where

$$C_m^{\text{calc}} = \frac{2 - x}{8} (\mu_{\text{so}}^{\text{Ni}})^2 + \frac{x}{8} (\mu_{\text{so}}^{\text{Cu}})^2$$

Here the $\mu_{\text{so}}^{\text{Ni}}$ and $\mu_{\text{so}}^{\text{Cu}}$ represent the spin-only effective moments of the Ni^{2+} and Cu^{2+} . The temperature and frequency dependences of the ac molar susceptibilities of $\text{La}_3\text{Ni}_{1.75}\text{Cu}_{0.25}\text{B}'\text{O}_9$ ($\text{B}' = \text{Sb}, \text{Ta}$ or Nb) and $\text{La}_3\text{Ni}_{1.5}\text{Cu}_{0.5}\text{NbO}_9$ are shown in Fig. 7. The real component, χ' , has a maximum at the temperature where χ_{dc} rises significantly and χ'' has a maximum at the same temperature or a slightly lower temperature. Moreover, for all compositions other than $\text{La}_3\text{Ni}_{1.75}\text{Cu}_{0.25}\text{NbO}_9$, a secondary maximum in χ'' is observed at $\sim 60 \text{ K}$. Note that $d\chi''/d\omega$ is positive at the principal maximum and negative at the secondary maximum. The field dependence of the magnetisation per formula unit, $M(H)$, of each compound is shown in Fig. 8. In no case is hysteresis apparent at either 150 or 220 K although $M(H)$ is always nonlinear at 150 K. However, hysteresis is present at 5 K in each compound and the values of the coercive field (H_c) and remanent magnetisation (M_R) observed at this temperature are included in Table 6. For each perovskite, $M(H)$ was also recorded at the temperature at which a local minimum was observed in the imaginary component of the ac magnetic susceptibility. Hysteresis was less apparent at these temperatures, especially in the case of $\text{La}_3\text{Ni}_{1.75}\text{Cu}_{0.25}\text{NbO}_9$.

The B/B'-site distribution determined at room temperature was held constant during the Rietveld analyses of the neutron diffraction patterns

Table 4Selected bond lengths (Å) and angles (°) in $\text{La}_3\text{Ni}_{1.75}\text{Cu}_{0.25}\text{B}'\text{O}_9$ at RT and 3 K.

	$\text{B}' = \text{Sb}$		$\text{B}' = \text{Ta}$		$\text{B}' = \text{Nb}$	
	RT	3 K	RT	3 K	RT	3 K
La–O1	2.745(10)	2.736(8)	2.701(9)	2.754(8)	2.7528(1)	2.701(8)
La–O1	2.726(9)	2.710(8)	2.751(8)	2.710(7)	2.7158(1)	2.742(6)
La–O1	2.450(8)	2.441(6)	2.418(7)	2.463(8)	2.4692(1)	2.417(7)
La–O2	2.849(11)	2.839(8)	2.882(9)	2.793(9)	2.8086(1)	2.835(9)
La–O2	2.445(8)	2.437(7)	2.465(8)	2.435(8)	2.4331(1)	2.473(7)
La–O2	2.631(9)	2.635(8)	2.608(9)	2.648(9)	2.6479(1)	2.612(7)
La–O3	2.554(3)	2.535(2)	2.554(3)	2.532(3)	2.5384(1)	2.532(2)
La–O3	2.437(4)	2.426(3)	2.429(5)	2.419(4)	2.4273(1)	2.417(3)
2c – O1	2.060(5)	2.059(5)	2.051(7)	2.057(5)	2.06096(4)	2.056(4)
2c – O2	2.068(5)	2.066(5)	2.061(7)	2.061(6)	2.0653(1)	2.052(5)
2c – O3	2.071(9)	2.040(8)	2.066(8)	2.085(12)	2.0806(1)	2.054(9)
2d – O1	2.014(5)	2.009(5)	2.021(6)	2.026(5)	2.0179(1)	2.027(4)
2d – O2	2.015(5)	2.023(6)	2.029(8)	2.023(6)	2.01558(4)	2.021(5)
2d – O3	1.997(9)	2.028(8)	2.000(8)	1.975(12)	1.9808(1)	2.003(9)
O1 – 2c – O2	89.5(3)	89.1(4)	89.9(4)	88.2(3)	88.742(2)	88.3(3)
O1 – 2c – O3	88.6(2)	88.4(2)	88.6(2)	88.9(2)	88.667(4)	88.9(2)
O2 – 2c – O3	88.0(2)	88.5(2)	88.1(2)	88.0(2)	87.791(5)	88.4(2)
O1 – 2d – O2	87.4(3)	88.8(4)	88.3(4)	86.6(3)	87.037(2)	86.8(3)
O1 – 2d – O3	89.4(2)	89.8(2)	89.4(2)	89.4(2)	89.430(6)	89.5(2)
O2 – 2d – O3	89.4(2)	89.5(2)	89.4(2)	90.0(2)	89.600(4)	89.8(2)
2c – O1 – 2d	154.8(3)	155.0(3)	155.0(4)	153.1(3)	153.984(1)	153.0(3)
2c – O2 – 2d	153.6(3)	152.4(3)	152.8(4)	154.2(4)	153.744(1)	154.1(3)
2c – O3 – 2d	154.3(2)	153.6(1)	154.0(2)	153.9(1)	154.291(1)	153.9(1)

collected at lower temperatures using both $\lambda = 1.622$ and 2.4395 Å. The shorter wavelength was used to deduce the structural parameters whereas the data collected using the longer wavelength provided better counting statistics for the refinement of the magnetic structure. The patterns collected at 3 K and the calculated fits are presented in Figs. 9 and S5 – S7. In preliminary refinements the displacement parameters, U_{ISO} , of some oxide anions became negative. However, the values were within one standard deviation of zero and they were therefore fixed at that value in subsequent refinements. The atomic parameters, together with some selected bond lengths and bond angles, are included in Tables 2 – 5, S1 and S2. Additional intensity was seen in the 011 reflection of the perovskite phase below the magnetic transition temperature for all compounds using both wavelengths, and hence it was assumed to be magnetic in origin. This extra scattering could be accounted for by adding a G-type magnetic structure with the ordered moments aligned along

Table 5Selected bond lengths (Å) and angles (°) in $\text{La}_3\text{Ni}_{1.5}\text{Cu}_{0.5}\text{NbO}_9$ at RT and 3 K.

	RT	3 K
La–O1	2.714(7)	2.691(5)
La–O1	2.743(6)	2.749(5)
La–O1	2.445(6)	2.416(5)
La–O2	2.831(8)	2.848(6)
La–O2	2.449(6)	2.465(5)
La–O2	2.639(7)	2.607(5)
La–O3	2.541(2)	2.524(2)
La–O3	2.422(3)	2.412(3)
2c – O1	2.079(5)	2.067(4)
2c – O2	2.076(5)	2.058(4)
2c – O3	2.014(9)	2.004(7)
2d – O1	2.002(5)	2.019(4)
2d – O2	2.015(6)	2.028(5)
2d – O3	2.053(9)	2.060(7)
O1 – 2c – O2	89.3(3)	88.7(2)
O1 – 2c – O3	87.9(1)	88.0(1)
O2 – 2c – O3	88.6(2)	88.4(2)
O1 – 2d – O2	87.7(3)	87.2(2)
O1 – 2d – O3	89.4(2)	89.6(1)
O2 – 2d – O3	89.4(2)	89.7(1)
2c – O1 – 2d	154.2(2)	153.2(2)
2c – O2 – 2d	153.1(3)	153.1(3)
2c – O3 – 2d	153.7(1)	153.1(1)

[100]. The magnetic structure has 100% and 33% magnetic occupancy of the 2c and 2d sites, respectively. When two magnetic cations occupy the same site, the only quantity that can be determined is the mean magnetic moment, M_{O} , per site; no partition between the two disordered species can be derived from the data. The magnetic form factor of Ni^{2+} was therefore used for all the magnetic cations and they were all assumed to have the same atomic moment, see Table 6. An additional NPD dataset was collected from $\text{La}_3\text{Ni}_{1.75}\text{Cu}_{0.25}\text{TaO}_9$ at 95 K using $\lambda = 2.4395$ Å. The pattern could be fitted, see Fig. S8, using the magnetic model used to account for the data collected at 3 K. The mean magnetic moment per site at 95 K was found to be $0.7(1) \mu_{\text{B}}$.

4. Discussion

The data described above show that it is possible to substitute at least 12.5% of the Ni^{2+} cations in $\text{La}_3\text{Ni}_2\text{B}'\text{O}_9$ with Cu^{2+} when $\text{B}' = \text{Sb}$, Ta or Nb. The space-group symmetry of the structure does not change when Cu^{2+} is introduced and the samples retain a high degree of crystallinity, as judged by both neutron diffraction and electron diffraction. The Cu^{2+} cations share the 2c site with Ni^{2+} cations when $x = 0.25$, see Fig. 4, but the neutron diffraction data collected from $\text{La}_3\text{Ni}_{1.5}\text{Cu}_{0.5}\text{NbO}_9$ show that as their concentration increases they also occupy the 2d site, albeit in smaller numbers, see Table 3. The mean cation – to – oxygen bond lengths around the 2c sites, see Table 4, are, as expected, always longer than those around the 2d site and they are relatively insensitive to the identity of B' when $x = 0.25$. Most noticeably, the pseudo-tetragonal compression of the coordination polyhedron seen in $\text{La}_3\text{Ni}_2\text{NbO}_9$ and $\text{La}_3\text{Ni}_2\text{TaO}_9$ [6] is not observed at room temperature in the $x = 0.25$ compositions. It is, however, restored when $x = 0.5$, see Table 5. It is impossible to interpret these apparent changes in detail for a number of reasons. Firstly, both sites are occupied by more than one type of cation and the tabulated bond lengths are therefore only mean values. Furthermore, our analysis of the angular dependence of the background scattering observed in the diffraction pattern of $\text{La}_3\text{Ni}_2\text{SbO}_9$ [21] and the diffuse scattering observed in the electron diffraction patterns collected from $\text{La}_3\text{Ni}_2\text{TaO}_9$ and $\text{La}_3\text{Ni}_2\text{NbO}_9$ [6] suggests that the distribution of the cations over 2d sites in these materials is not always random on a local distance scale. The tendency of Cu^{2+} to occupy a distorted coordination environment as a consequence of the otherwise-degenerate electron configuration of a d^9 cation must also be considered. However, this

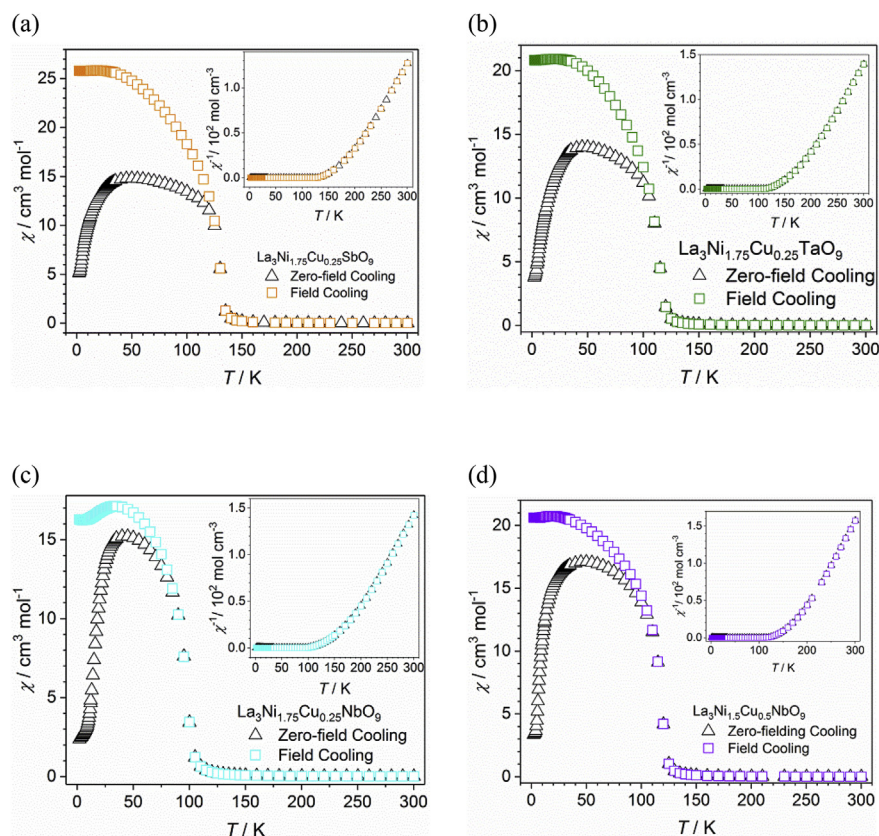


Fig. 6. Temperature dependence of the dc molar susceptibility and inverse susceptibility of (a) $\text{La}_3\text{Ni}_{1.75}\text{Cu}_{0.25}\text{SbO}_9$, (b) $\text{La}_3\text{Ni}_{1.75}\text{Cu}_{0.25}\text{TaO}_9$, (c) $\text{La}_3\text{Ni}_{1.75}\text{Cu}_{0.25}\text{NbO}_9$ and (d) $\text{La}_3\text{Ni}_{1.5}\text{Cu}_{0.5}\text{NbO}_9$.

usually results in the formation of two long bonds and four short bonds in the octahedron of coordinating oxide ions, and no cooperative distortion of this type is seen around the copper-rich 2c sites in any of the compounds included in this study. However, we cannot rule out the possibility that uncorrelated, local distortions are present within the structure. The tendency of the $d^0 \text{Nb}^{5+}$ and Ta^{5+} cations to move away from the centre of their octahedra [22] could be an equally important factor in determining the local structure. The likely presence of some combination of these local deviations from the mean structure limits the depth to which the bond lengths derived from a neutron diffraction experiment can be interpreted.

The dc magnetometry data shown in Figs. 6 and 8 suggest that each of the four compounds studied undergoes a transition to a ferromagnetic state on cooling through the temperature range $90 \leq T/\text{K} \leq 130$ and the ac data shown in Fig. 7 are consistent with this conclusion. However, the frequency and temperature dependencies of the latter data below the Curie temperature, T_C , show that none of these compounds is a simple ferromagnet. The observation of magnetic Bragg scattering in the neutron diffraction pattern collected from $\text{La}_3\text{Ni}_{1.75}\text{Cu}_{0.25}\text{TaO}_9$ argues against the existence of a re-entrant spin-glass phase at 95 K and the neutron diffraction patterns recorded at 3 K prove that long-range magnetic ordering is always present at that temperature. The G-type structure

used to model the data involves antiferromagnetic coupling between spins on nearest-neighbour sites and, as discussed above, the resultant magnetisation is a consequence of there being different concentrations of magnetic cations on these sites. These compounds could therefore be described as ferrimagnets rather than ferromagnets but we shall continue to use the latter term. Each composition has a magnetisation of $\sim 1.5 \mu_B$ per formula unit in 50 kOe at 5 K. However, the ordered moment determined by neutron diffraction varies by $\sim 33\%$ across the series, see Table 6. It therefore seems likely that, as in the case of $\text{La}_3\text{Ni}_2\text{SbO}_9$ [2], long-range ordered regions coexist with ordered domains that are too small to contribute to the magnetic Bragg scattering, although they can be aligned with the net magnetisation by an applied field. Our crystallites thus consist of relatively-large, long-range ordered regions interspersed with smaller relaxor regions. The nature of the domain walls between these two types of region is still under investigation but their movement might be responsible for the unusual behaviour of the ac susceptibility at temperatures well below T_C .

The presence of only 12.5% Cu^{2+} has a remarkable effect on the behaviour of these Ni^{2+} -based oxides. The changes are least marked when $B' = \text{Sb}$; $\text{La}_3\text{Ni}_2\text{SbO}_9$ has been shown to have a backbone of long-range ordered spins with relaxor domains also present and the neutron diffraction and magnetometry data collected from $\text{La}_3\text{Ni}_{1.75}\text{Cu}_{0.25}\text{SbO}_9$

Table 6
Magnetic parameters of $\text{La}_3\text{Ni}_{2-x}\text{Cu}_x\text{B}'\text{O}_9$.

B'	x	C_m^{calc}	C_m	θ_W/K	H_C/kOe	M_R/μ_B	T_C/K	T_{MAX}/K	M_O/μ_B^a
Sb	0.25	1.84	1.05(1)	+169(4)	0.2	0.38	130	50	1.22(4)
Ta	0.25	1.84	1.01(1)	+161(3)	0.32	0.18	110	45	1.15(5)
Nb	0.25	1.84	1.02(1)	+156(3)	0.35	0.42	90	45	0.94(6)
Nb	0.5	1.69	0.87(1)	+165(4)	0.2	0.3	110	50	0.83(6)

^a The mean ordered magnetic moment per cation, determined by neutron diffraction, in $\text{La}_3\text{Ni}_{2-x}\text{Cu}_x\text{B}'\text{O}_9$ at 3 K.

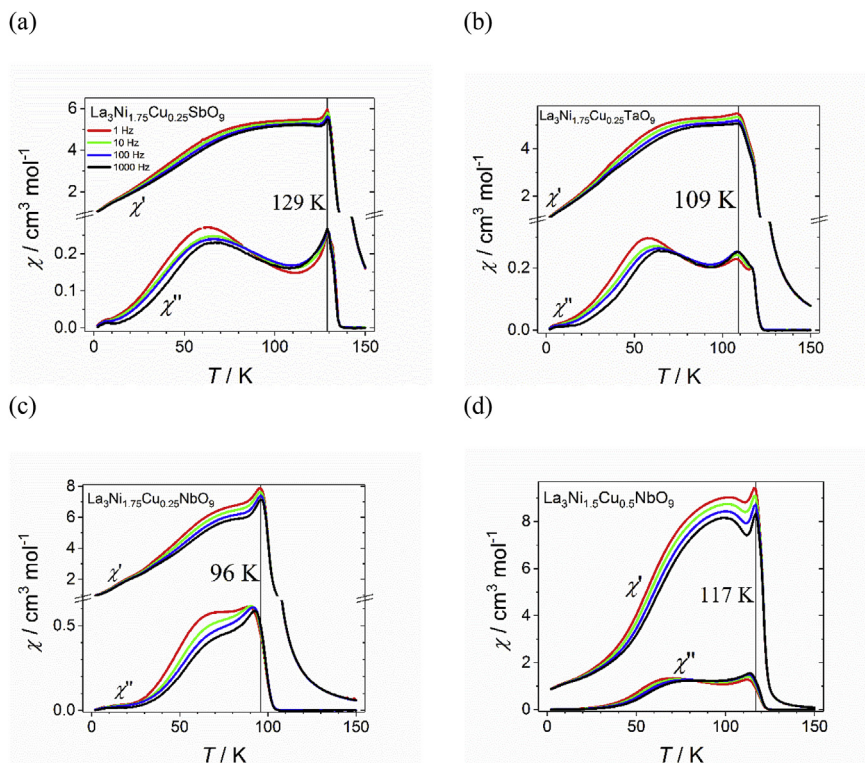


Fig. 7. Temperature and frequency dependence of the real and imaginary components of the ac molar susceptibility of (a) $\text{La}_3\text{Ni}_{1.75}\text{Cu}_{0.25}\text{SbO}_9$, (b) $\text{La}_3\text{Ni}_{1.75}\text{Cu}_{0.25}\text{TaO}_9$, (c) $\text{La}_3\text{Ni}_{1.75}\text{Cu}_{0.25}\text{NbO}_9$ and (d) $\text{La}_3\text{Ni}_{1.5}\text{Cu}_{0.5}\text{NbO}_9$ collected at 1 (red), 10 (green), 100 (blue) and 1000 (black) Hz. (For interpretation of the references to colour in this figure legend, the reader is referred to the Web version of this article.)

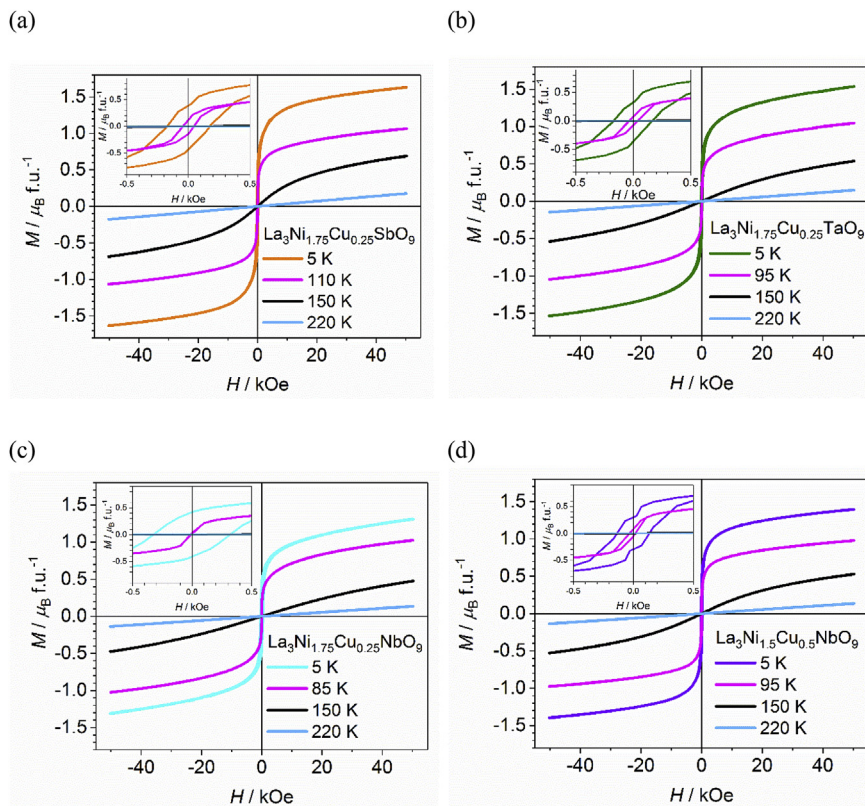


Fig. 8. Field dependence of the magnetisation per formula unit of (a) $\text{La}_3\text{Ni}_{1.75}\text{Cu}_{0.25}\text{SbO}_9$, (b) $\text{La}_3\text{Ni}_{1.75}\text{Cu}_{0.25}\text{TaO}_9$, (c) $\text{La}_3\text{Ni}_{1.75}\text{Cu}_{0.25}\text{NbO}_9$ and (d) $\text{La}_3\text{Ni}_{1.5}\text{Cu}_{0.5}\text{NbO}_9$ at four different temperatures. The insets show the same function for a smaller range of H .

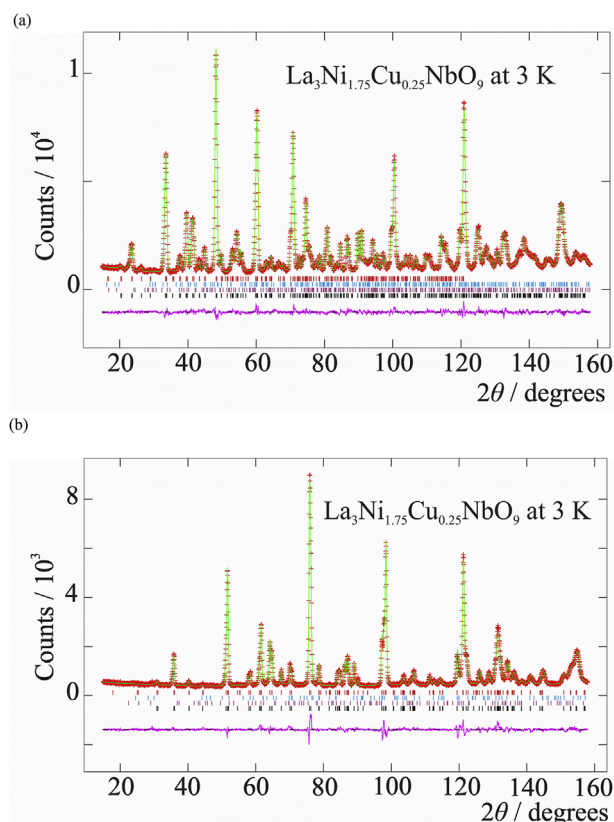


Fig. 9. Observed (red crosses) and calculated (green line) NPD profiles of $\text{La}_3\text{Ni}_{1.75}\text{Cu}_{0.25}\text{NbO}_9$ at 3 K using $\lambda =$ (a) 1.622 and (b) 2.4395 Å. A difference curve (purple) is shown below. Reflection markers are shown for the magnetic (red) and structural (black) perovskite phases, LaNbO_4 (cyan) and La_3NbO_7 (purple). (For interpretation of the references to colour in this figure legend, the reader is referred to the Web version of this article.)

can be interpreted using a similar model. However, the imaginary component of the ac susceptibility of the copper-free composition does not show a local maximum below T_C and the introduction of 12.5% Cu^{2+} increases the Curie temperature by ~ 30 K. More significant changes are seen in the tantalum-based system, wherein, in addition to an enhancement of T_C , the introduction of Cu^{2+} is accompanied by the formation of regions showing long-range magnetic order in addition to the relaxor regions found in the Cu-free composition. The most dramatic changes are seen in $\text{La}_3\text{Ni}_{2-x}\text{Cu}_x\text{NbO}_9$. $\text{La}_3\text{Ni}_2\text{NbO}_9$ is a spin glass with $T_g \sim 29$ K. The introduction of 12.5% (25%) Cu^{2+} causes the onset of long-range G-type magnetic ordering and increases the magnetic transition temperature to 96 K (117 K). In order to eliminate the spin-glass behaviour it is necessary to eliminate or reduce the frustration that causes it. We previously discussed the source of the frustration in $\text{La}_3\text{Ni}_2\text{NbO}_9$ and concluded that it is most likely to arise from the presence of $180^\circ \text{Ni}-\text{O}-\text{Nb}-\text{O}-\text{Ni}$ interactions that compete with $\text{Ni}-\text{O}-\text{Ni}$ interactions. When $x = 0.25$, the presence of Cu^{2+} introduces $180^\circ \text{Cu}-\text{O}-\text{Ni}$, $\text{Cu}-\text{O}-\text{Nb}-\text{O}-\text{Ni}$ and $\text{Cu}-\text{O}-\text{Nb}-\text{O}-\text{Cu}$ interactions; further interactions are introduced when Cu^{2+} cations also partially occupy the 2d sites, as in $\text{La}_3\text{Ni}_{1.5}\text{Cu}_{0.5}\text{NbO}_9$. As a consequence of the different electron configurations of Ni^{2+} and Cu^{2+} , the introduction of the latter cation will lead to changes in the magnitude and, sometimes, the sign of the relevant exchange constants. Any local variations in the bond lengths around the Jahn-Teller-active Cu^{2+} cations will also have consequences for the magnetic interactions. It is thus easy to understand why the magnetic behaviour might change but, with the data available, very difficult to predict or rationalise the nature of the changes in these heavily disordered compounds. Vasala et al. [20] have previously described the consequences of a Jahn-Teller distortion for the magnetic properties of double perovskites

containing Cu^{2+} and Mustonen et al. [23] and Katukuri et al. [24] have discussed the changes that occur in those materials when a d^0 diamagnetic cation is replaced by a d^{10} cation. The compounds described in this paper are subject to both these factors, with cation disorder present as an additional complication.

5. Conclusion

The introduction of Cu^{2+} cations into $\text{La}_3\text{Ni}_2\text{B}'\text{O}_9$ ($\text{B}' = \text{Sb}, \text{Ta}, \text{Nb}$) has a marked effect on the magnetic properties. In the case where $\text{B}' = \text{Sb}$ the substituted composition is similar to the parent material [1,2] in that, at low temperatures, it contains regions that show long-range magnetic order and regions that appear to show relaxor behaviour. The evidence for this comes from magnetometry and neutron diffraction and includes the observation that the ordered moment measured by neutron diffraction is very low compared to the magnetisation measured by magnetometry. The most striking consequence of the substitution in this case is that T_C increases by ~ 30 K. $\text{La}_3\text{Ni}_2\text{TaO}_9$ is a relaxor ferromagnet [6], the low-temperature neutron diffraction pattern of which shows no evidence of long-range magnetic order. Following the introduction of 12.5% Cu^{2+} , $\text{La}_3\text{Ni}_{1.75}\text{Cu}_{0.25}\text{TaO}_9$ shows long-range magnetic order at a temperature ~ 30 K higher than that at which the copper-free composition begins to behave as a relaxor ferromagnet. However, as in the case $\text{B}' = \text{Sb}$, the experimental evidence suggests that ordered and relaxor regions coexist below the transition temperature. The most dramatic changes are seen when $\text{B}' = \text{Nb}$, in which case the introduction of Cu^{2+} transforms the spin-glass parent composition into a mixed magnetically-ordered/relaxor phase. Although the origins of all these changes remain to be elucidated, our data demonstrate again the sensitivity of the magnetic properties of these perovskites to chemical composition.

Acknowledgments

We thank EPSRC for funding through grant EP/M0189541. CMC thanks the Croucher Foundation and the University of Oxford for the award of a graduate scholarship.

Appendix A. Supplementary data

Supplementary data to this article can be found online at <https://doi.org/10.1016/j.jssc.2019.05.006>.

References

- [1] P.D. Battle, S.I. Evers, E.C. Hunter, M. Westwood, *Inorg. Chem.* 52 (2013) 6648–6653.
- [2] P.D. Battle, M. Avdeev, J. Hadermann, *J. Solid State Chem.* 220 (2014) 163–166.
- [3] P.K. Davies, M.A. Akbas, *J. Phys. Chem. Solids* 61 (2000) 159–166.
- [4] R. Paria Sena, J. Hadermann, C.M. Chin, E.C. Hunter, P.D. Battle, *J. Solid State Chem.* 243 (2016) 304–311.
- [5] C.M. Chin, R. Paria Sena, E.C. Hunter, J. Hadermann, P.D. Battle, *J. Solid State Chem.* 251 (2017) 224–232.
- [6] C.M. Chin, P.D. Battle, S.J. Blundell, E. Hunter, F. Lang, M. Hendrickx, R.P. Sena, J. Hadermann, *J. Solid State Chem.* 258 (2018) 825–834.
- [7] K. Dey, A. Indra, D. De, S. Majumdar, S. Giri, *ACS Appl. Mater. Interfaces* 8 (2016) 12901–12907.
- [8] E.C. Hunter, P.D. Battle, R. Paria Sena, J. Hadermann, *J. Solid State Chem.* 248 (2017) 96–103.
- [9] Y.W. Tang, E.C. Hunter, P.D. Battle, M. Hendrickx, J. Hadermann, J.M. Cadogan, *Inorg. Chem.* 57 (2018) 7438–7445.
- [10] D.G. Franco, V.C. Fustes, M.C. Blanco, M.T. Fernandez-Diaz, R.D. Sanchez, R.E. Carbonio, *J. Solid State Chem.* 194 (2012) 385–391.
- [11] C.M. Chin, P.D. Battle, E.C. Hunter, M. Avdeev, M. Hendrickx, J. Hadermann, *J. Solid State Chem.* 273 (2019) 175–185.
- [12] M. Avdeev, J.R. Hester, *J. Appl. Crystallogr.* 51 (2018) 1597–1604.
- [13] H.M. Rietveld, *J. Appl. Crystallogr.* 2 (1969) 65–71.
- [14] A.C. Larson, R.B. von Dreele, *General Structure Analysis System (GSAS)* Los Alamos National Laboratories LAUR 86-748, 1994.
- [15] H.J. Rossel, *J. Solid State Chem.* 27 (1979) 115.
- [16] K.P.F. Siqueira, R.M. Borges, E. Granado, L.M. Malard, A.M. de Paula, R.L. Moreira, E.M. Bittar, A. Dias, *J. Solid State Chem.* 203 (2013) 326–332.

- [17] F. Vullum, F. Nitsche, S.M. Selbach, T. Grande, J. Solid State Chem. 181 (2008) 2580–2585.
- [18] M. Wakeshima, H. Nishimine, Y. Hinatsu, J. Phys. Condens. Matter 16 (2004) 4103–4120.
- [19] M.T. Anderson, K.B. Greenwood, G.A. Taylor, K.R. Poeppelmeier, Prog. Solid State Chem. 22 (1993) 197–233.
- [20] S. Vasala, M. Karppinen, Prog. Solid State Chem. 43 (2015) 1–36.
- [21] C.M. Chin D. Phil Thesis, Oxford, 2019.
- [22] K.M. Ok, P.S. Halasyamani, D. Casanova, M. Llunell, P. Alemany, S. Alvarez, Chem. Mater. 18 (2006) 3176–3183.
- [23] O. Mustonen, S. Vasala, K.P. Schmidt, E. Sadrollahi, H.C. Walker, I. Terasaki, F.J. Litterst, E. Baggio-Saitovitch, M. Karppinen, Phys. Rev. B 98 (2018), 064411.
- [24] V.M. Katukuri, P. Babkevich, O. Mustonen, H.C. Walker, B. Fak, S. Vasala, M. Karppinen, H.M. Ronnow, O.V. Yazyev. <https://arxiv.org/abs/1902.09376>, 2019.